Atomic structures of an entire contractile injection system in both the extended and contracted states

Ambroise Desfosses, H Venugopal, T Joshi, Jan Felix, M Jessop, H Jeong, J Hyun, J. Bernard Heymann, Mark R. H. Hurst, Irina Gutsche, et al.

Atomic structures of an entire contractile injection system in both the extended and contracted states

Ambroise Desfosses[1,2], **Hariprasad Venugopal**[1,3], **Tapan Joshi**[1], **Jan Felix**, **Matthew Jessop**[1,2], **Hyengseop Jeong**[4], **Jaekyung Hyun**[4,5], **J. Bernard Heymann**[6], **Mark R. H. Hurst**[7,8,*], **Irina Gutsche**[2,*], **Alok K. Mitra**[1,*]

[1]School of Biological Sciences, University of Auckland, Thomas Building, 3A Symonds Street, Auckland, New Zealand [2]Institut de Biologie Structurale, Univ. Grenoble Alpes, CEA, CNRS, IBS, 71 Avenue des martyrs, F-38044 Grenoble, France [3]Ramaciotti Centre for Cryo Electron Microscopy, Monash University, Wellington Rd, Clayton VIC 3800, Melbourne, Australia [4]Electron Microscopy Research Center, Korea Basic Science Institute, 162 Yeongudanji-ro, Ochang-eup, Cheongwon-gu, Cheongju-si, Chungcheongbuk-do 28119, Republic of Korea [5]Molecular Cryo-Electron Microscopy Unit, Okinawa Institute of Science and Technology Graduate University, 1919-1 Tancha, Onna, Kunigami District, Okinawa 904-0412, Japan [6]Laboratory for Structural Biology Research, National Institute of Arthritis, Musculoskeletal, and Skin Diseases, National Institutes of Health, Bethesda, MD 20892, USA [7]Forage Science, AgResearch, Lincoln Research Centre, Christchurch, New Zealand [8]Bio-Protection Research Centre, Lincoln, Christchurch, New Zealand

Abstract

Contractile injection systems are sophisticated multiprotein nanomachines that puncture target cell membranes. While the amount of atomic resolution insights into contractile bacteriophage tails, bacterial type six secretion systems and R-pyocins is rapidly increasing, structural information about contraction of bacterial phage-like protein-translocation structures directed towards eukaryotic hosts is scarce. Here we characterise the antifeeding prophage AFP from *Serratia*

*Correspondence and request for materials should be addressed to AKM, IG and MRHH.

ORCID for corresponding authors
IG ORCID identifier is 0000-0002-1908-3921
AM ORCID identifier is 0000-0003-0891-5697
MH ORCID identifier is 0000-0001-5826-5253

entomophila by cryo-electron microscopy. We present the high-resolution structure of the entire AFP particle in the extended state, trace 11 protein chains *de novo* from the apical cap to the needle tip, describe localisation variants and perform specific structural comparisons with related systems. We analyse intersubunit interactions and highlight their universal conservation within contractile injection systems while revealing the specificities of AFP. Furthermore, we provide the structure of the AFP sheath-baseplate complex in a contracted state. This study reveals atomic details of interaction networks that accompany and define the contraction mechanism of toxin-delivery tailocins, offering a comprehensive framework for understanding their mode of action and for their possible adaptation as biocontrol agents.

Background

Contractile injection systems (CIS) consist of a long tube with a needle-like tip, a helical sheath surrounding the tube, and a baseplate linking external signals with sheath contraction that propels the tube out of the sheath, enabling the needle to perforate the target membrane[1,2]. In addition to contractile bacteriophage tails, CIS include bacterial contractile phage tail-like particles (CPTPs)[3], further subdivided into intracellular Type VI secretion system (T6SS)[4–6] and extracellular CIS (eCIS). The latter includes R-pyocins[7–9] that dissipate proton motive force of their target bacteria, as well as phage-like protein-translocation structures (PLTS)[10–12] that inject specific toxic proteins into eukaryotic cells. This major difference with pyocins led to PLTS qualification as toxin-delivery tailocins[3,13] thereby emphasising their relationship with both pyocins and T6SS[4–6]. These systems, bioinformatically identified in hundreds of bacteria and archaea dwelling in different environments[12] are exemplified by the *Serratia* antifeeding prophage (AFP)[10,13] and the *Photorhabdus* virulence cassette (PVC)[11,14], targeting insect larvae and haemocytes respectively, and similar to the metamorphosis-associated contractile structures (MACs)[15] and to the intracellular *Amoebophilis asiaticus* CIS[6,16].

The cryo-electron microscopy (cryo-EM) "revolution" has enabled spectacular progress in structural characterisation of both T6SS and R-pyocin, as well as of the related myophage T4[9,17–20]. However, structural understanding of PLTS is lagging behind, with only a single recent publication detailing the structures of the entire extended PVC particle and the contracted PVC sheath[14]. Here, we present high-resolution structures of AFP, the archetype PLTS from the soil bacterium *Serratia entomophila* [10,13] in both extended and contracted states, including the previously unknown structure of a contracted PLTS baseplate. This analysis enables us to propose a structural mechanism of AFP action as a toxin-delivery syringe, and to provide a detailed comparison with other CIS. Conservation of the baseplate components among the PLTS suggests that the inferred contraction mechanism is likely shared by all toxin-delivery tailocins.

Results

The overall structure of the AFP particle

The *S. entomophila* AFP gene cluster comprises 18 open reading frames with translation products denoted as Afp1 to Afp18[10] (Supplementary Table 1). AFP translocates the

insecticidal toxin Afp18 into larvae of the New Zealand pasture pest *Costelytra giveni*, thereby causing cessation of feeding activity[10,21]. The extended AFP is a ~110 nm long bullet-shaped particle, built up by a helical trunk with a conical cap at the apical end and a flat base with a mobile fibre network at the proximal end (Fig. 1). In order to obtain a high-resolution cryo-EM structure of the entire AFP particle, its images were divided into three parts – the trunk (containing the sheath and inner tube), the cap and the baseplate. Each part was reconstructed separately and recombined to give a final composite cryo-EM map (see Methods, Fig. 1a,b,d Supplementary Fig. 1, 2, Supplementary Table 2). This approach allowed us to (i) benefit from the helical symmetry of the trunk while applying a six-fold or three-fold rotational symmetry to the baseplate and needle and a six-fold symmetry to the cap, and (ii) circumvent long-range distortions and separate two populations of AFP particles that differ in terms of the trunk length (Fig. 1a, Supplementary Fig. 1, 2). The resolution of most of the structure ranges from 2.8 to 3.3 Å, which is overall slightly higher than the recently published PVC structure[14], and falls off towards the peripheral trunk protrusions, baseplate edges and attachment fibres (Fig. 1d,e Supplementary Fig. 3, Supplementary Table 2). *De novo* atomic model building for nearly all proteins composing the AFP particle (Supplementary Table 3) was made possible by the high quality of the maps (Fig. 1, Supplementary Fig. 3) which reflects the regularity of the assembly, and especially of the best-resolved inner tube which needs to be rigid enough to penetrate the cell membrane upon contraction. In the contracted state (Fig. 1f, Supplementary Fig. 2, 4, 6), the length of the sheath decreases from 850 to 350 Å and the diameter swells from 170 to 230 Å to eject the inner tube through a rearranged baseplate. The post-contraction baseplate (5.4 Å global resolution, ranging from ~4 Å for the bottom of the sheath to ~12 Å for the outer rim of the baseplate) is less well resolved than the sheath (3.8 Å resolution), presumably because of the loss of the needle-baseplate interactions required for the tube and needle release.

The final atomic model of the extended AFP contains a total of 11 different proteins. Three proteins make up the inner tube (Afp1, Afp5 and Afp7), three others build the surrounding sheath (Afp2, Afp3 and Afp4), two comprise the needle (Afp10 and Afp8), three belong to the baseplate (Afp9, Afp11 and Afp12), and one constitutes the apical cap (Afp16) (Fig. 1 a,b,g). The fibres formed by Afp13 are not well resolved (Fig. 1e, Supplementary Fig. 3), which is consistent with their proposed function in sensing the target cell surface[10], requiring mobility and flexibility to orient the AFP particle and position the baseplate for the power stroke[2]. Mass-spectrometry measurements (see Methods and Supplementary Table 1) identified a single copy of the Afp18 toxin, presumably represented by an unassigned density inside the tube, as well as the small and uncharacterised Afp6, which may either be also inside the tube, or at the baseplate periphery associated with fibres. These measurements also confirmed the absence of the tape measure protein Afp14[22,23], the assembly chaperone AAA+ ATPase Afp15[22] and the "inactive pseudotoxin" Afp17[22,24] in the mature particle.

The AFP tube

As in the phage T4[20], the first ring of the AFP tube is assembled at the baseplate from Afp7 (equivalent of gp48), followed by a ring of Afp5 (eq. gp54) and subsequent rings of Afp1 that span the interior of the entire particle up to the apical end formed by the tail tube

terminator cap of Afp16 (eq. gp15) (Fig. 1a, Fig. 2). Afp1, Afp5 and Afp7 have a common fold (Fig. 2b) shared also with the T4 gp19, the T6SS Hcp and the R-pyocin, phage Lambda gpV[25] and T5 pb6[26] tube protein (Supplementary Fig. 5 a, b). Similarly to T4 gp19, the inner surface of the tube formed by Afp1 is negatively charged, possibly to allow for efficient release of Afp18 toxin which, at pH 11 in the *C. giveni* larval gut[27], would be negatively charged (Supplementary Fig. 5c). Afp7, like Pvc7, possesses a LysM-like[28] peptidoglycan-binding domain (Fig. 2e,g,h) and links the C6 symmetry of the tube to the C3 symmetry of the needle protein Afp8 (Fig. 2f, Supplementary Fig. 9c). At the apical end, in the cap-bound conformation, the N-terminal Afp1 α-helix unfolds to follow the interdomain loop of Afp16 (Fig. 2b, c). Each apical Afp1 strongly binds the cap by interacting with three Afp16 subunits, presumably to prevent the tube release from the opposite end upon contraction (see also below).

The β-hairpins of adjacent tube subunits constitute a β-sheet barrel of 75 nm in diameter in the middle of the tube. Each Afp1 monomer interacts with four subunits from the Afp1 layer above and four subunits from the layer below (Fig. 2d), the main interaction occurring via β-sheet intercalation as in the other CIS[9,29,30], and a continuous mesh of such β-sheet intercalations spreads through the entire particle, from the needle to the cap (Fig. 2c-f). The free energy of these tube-stabilising interactions and comparisons between intra-tube, intra-sheath and tube-sheath interactions in AFP, R-Pyocin and T6SS are detailed in Supplementary Tables 4 and 5. The observation that the intra-tube interactions, of similar strength in all three assemblies, are much stronger than the consistently weak tube-sheath interactions reflects the need for the rigidity of the tube upon perforation of the target cell, and the necessity for the tube to slide through the sheath during contraction.

The AFP sheath

The most striking feature of the AFP sheath is that it is constructed of two alternating hexameric layers, each composed of a different sheath protein[13] (Fig. 3). A comparative genomic study revealed that most of the PLTS contain one sheath encoding gene, while some have two and *Enterobacteria* (including *Serratia*) have three[12]. Afp2, Afp3 and Afp4 have a conserved fold (Fig. 3e, Supplementary Fig. 6) integrating elements of domains 1 and 2 of VipA-B/TssB-C[17]. At the proximal end, the sheath starts with a single hexameric ring of Afp4 followed by a ring of Afp2, and then Afp3 and Afp2 rings alternate up to the apical Afp16 cap. Approximately 77% of the AFP particles are built by 11 Afp2 and 10 Afp3 layers surrounding 21 layers of the tube protein Afp1 and resulting in a terminal Afp2-Afp16 interaction (Fig. 1a, Fig. 2a); ~23% contain only 10 Afp2 layers and 10 Afp3 layers surrounding 20 Afp1 layers, and therefore terminate with Afp3-Afp16 (Supplementary Fig. 1, 3). The tube-sheath interactions may be considered as identical along the length of the trunk, ignoring negligible differences in contacts between Afp1 and either Afp2 or Afp3 (Supplementary Fig. 6d).

Afp3 is the longest of the three sheath proteins and forms a poorly resolved N-terminal bulge responsible for the characteristic appearance of the AFP trunk[13], carved by six prominent ridges of Afp3 with deep Afp2 grooves in between (Fig. 1e, Supplementary Fig. 3d). In contrast to AFP, PVC has been described to be built of 10 layers of alternating Pvc2

and Pvc3 followed by 12 layers assembled exclusively of Pvc2[14]. However, examination of the entire PVC map (EMD-9762) suggests that this interpretation may have resulted from processing a mixed population of PVC particles, some of which may have been composed of Pvc2 and Pvc3 that actually alternated beyond the end of the back-folded fibres, further towards the apical cap, as is the case for AFP. Therefore, in addition to the fibre-docking function proposed based on the patterning of the PVC sheath[14], the N-terminal bulge domain of Afp3/Pvc3 may play another yet unidentified role. Noteworthy, the shape of this domain, which is partially conserved between Afp3 and Pvc3 (Supplementary Fig. 6f, g), is to some extent reminiscent of the slightly bigger domain 3 of VipA-B/TssB-C. However, the latter is known to be recognised by the cognate AAA+ ATPase ClpV in the contracted T6SS sheath to specifically trigger its disassembly and recycling[17,29,31], whereas in the PLTS the AAA+ ATPase is proposed to instead be involved in the assembly of the baseplate and the needle[22].

As in R-pyocins and T6SS, the sheath assembly appears to rely on a β-strand exchange in the innermost layer of the sheath, termed a "handshake" mechanism[9,17] (Fig. 3a, d). As described above for the intra-tube intercalations, the sheath-stabilising mesh of β-sheet handshakes propagates from the baseplate of the AFP particle to the cap (Fig. 3d). Indeed, Afp4 forms the first baseplate-proximal sheath ring by offering the corresponding β-strand to the sheath initiator Afp9 (eq. gp25) (Fig. 3d inset 4) while accepting an analogous β-strand of Afp2 which in turn, receives a β-strand from Afp3 (Fig. 3d inset 3), and this pattern continues up to the top-most sheath layer. Furthermore, in the cap, the tail-terminator Afp16 mimics this handshake interaction by binding into a cleft in the terminal Afp2/3 (Fig. 3d inset 1, see also below).

Although contraction was experimentally achieved by briefly subjecting AFP particles to GuHCl (see Methods), no loss of protein integrity was detected (Supplementary Fig. 6c). Similarly to R-pyocins[9], the handshake intersubunit connectivity does not change between the extended and the contracted state, presumably maintaining the sheath integrity (Fig. 3b, c, Supplementary Fig. 6a, b). Contraction leads to a rigid-body rotation of each sheath subunit roughly 33° and a 40 Å shift outwards, and the assembly length compresses by approximately two-fold. The switch from the extended to contracted state results in major displacements of the Afp2 and Afp3 N- and C-termini, with the Afp2 N-terminus rotating more than 120° (Fig. 3f). Upon contraction and radial expansion, the subunits of the upper rings insert in the newly formed gaps of the lower rings. Therefore, in spite of the loss of the contact with the tube, each sheath subunit buries ~900 Å^2 more of its surface (Supplementary Table 6), meaning that a total of ~730 kcal/mol of energy would be released during a single contraction resulting in the tube expulsion and drilling into the target cell membrane (Supplementary Tables 5, 6). Interestingly, the difference in free energy between the extended and contracted AFP sheath is much smaller than in T6SS and R-pyocin (Supplementary Table 5), probably reflecting the remarkable stability of extended AFP at basic pH in the host's gut.

The sheath-tube interaction appears universally conserved among CIS and mainly relies on complementary surface charges on contacting interfaces (see Supplementary Fig. 6d, e for conservation of Afp2 and Afp3 residues involved in Afp1 binding.) The fact that inside the

cell the AFP particle assembles into a metastable extended state may be explained by our earlier observation that the sheath polymerises on the already preassembled baseplate-tube scaffold[22], corroborated by the recent investigation of PVC mutants[14]. In the proposed directional assembly model, the tube polymerises on the preassembled baseplate until it reaches its optimal length controlled by the tape measure protein, and is then apically capped to prevent further growth and to prime the sheath loading[14,22]. The difference between the assembly mechanisms proposed for toxin-delivery tailocins, and for T6SS where the tube stays capped during growth,[32,33] may be explained by the unique nature of the PLTS cap and its mode of interaction.

The AFP apical end cap

Cryo-EM maps of the apex of the major and minor AFP populations are virtually identical, independent of whether the terminal layer under the Afp16 cap is comprised of Afp2 or Afp3 (Fig. 4, Supplementary Fig. 3c, f). The Afp16 protein is composed of two distinct domains linked by a long ß-strand containing loop, and forms a hexameric ring at the apex of the trunk. The N-terminal domain of Afp16, folded similarly to gp15 (T4)[34] and gpU (phage λ)[35] but differently from TssA (T6SS), constitutes an extra layer of the tube while the PLTS-specific C-terminal domain, slightly shifted inwards in AFP in comparison to PVC, caps the sheath (Fig. 4a-c, Supplementary Fig. 7a, b). The N-terminal Afp16 domains strongly bind to two Afp1 subunits underneath via a β-sheet intercalation, the linker ß-strand of Afp16 docks into the C-terminal domain of one Afp2 subunit in a handshake manner (Fig. 3 d panel 1, Fig. 4a, b), while the C-terminal Afp16 domain interacts with a neighbouring Afp2 and even stretches down to an Afp3 subunit one layer below (Fig. 4a, b). The N-terminal domain of Afp16 possesses a short α-helical insertion which, upon Afp16 hexamerisation, organises in a tight ring of 9 Å in diameter that constricts the extremity of the particle and likely ensures the directionality of the toxin egress through the baseplate and the needle (Fig. 4c, Supplementary Fig. 7a). Noteworthy, no capping of the AFP or PVC sheath was observed in the contracted state.

The AFP baseplate and the needle

The overall architecture of the AFP baseplate is similar to PVC and follows the same organisation as the conserved inner baseplate of phage T4 (Supplementary Fig. 8). In comparison with the sophisticated full T4 baseplate[20], which contains a complex tail fibre network, the AFP, PVC[14] and T6SS[36–38] baseplates are elegantly simple (Supplementary Fig. 8). In agreement with the other CIS, the AFP baseplate can be described as a C6-symmetrical assembly of sub-complexes historically called "wedges" that circularise around the C3-symmetrical needle[2]. The structure of the needle-baseplate complex (Fig. 5) was solved to an average of 3.1 Å resolution (see Methods and Supplementary Fig. 1 for details). As in T6SS VgrG[4], Afp8 is a fusion of the hub (eq. gp27) and the needle (eq. gp5) genes, while the tip of the needle is encoded by Afp10 (eq. gp5.4, VgrG PAAR in T6SS) (Supplementary Fig. 9e). Reminiscent of PVC, T4[39] and T6SS[40], the needle hub is composed of twin ß-barrel domains of Afp8 with a fold similar to the core domain of the tube proteins (Fig. 5b, c). This creates a pseudohexameric layout which accommodates the transition from the hexameric ring formed by the tube initiator Afp7 (eq. gp48) to the C3-symmetry of the rest of the Afp8 needle trimer (Supplementary Fig. 9c). Thus, the top

surface of Afp8 packed against the bottom of Afp7 plays the C6-to-C3 symmetry adaptor function attributed to gp27[20]. Interestingly, the similarity with gp27 extends even beyond the twin domains (Supplementary Fig. 9e). The bottom of Afp8 forms a tapered needle with an intercalated ß-helical wall analogous to the T4 gp5 and T6SS VgrG/VgrG1 but notably shorter; this difference in length (Supplementary Fig. 9e) may be related to the specificity of AFP for eukaryotic targets. The tip of the C3-symmetric needle is sharpened by a single copy of Afp10. Remarkably, the Afp8-bound region of Afp10 follows a pseudo-C3 symmetry, resulting in three clearly resolved ß-sheets characteristic of gp5.4, the T4 homologue of Afp10, and thus enabling fitting of gp5.4 into the density (Supplementary Fig. 9f).

The AFP wedge is comprised of the sheath initiator protein Afp9, featuring an EPR motif conserved over a variety of CIS (eq. gp25), and two other baseplate proteins, Afp11 and Afp12 (Fig. 5e, f). In contrast, the T4 wedge is composed of gp25, gp53 and a module built of two copies of gp6 and one copy of gp7 stabilised by an α-helical core bundle[20]. Despite these apparent differences, both wedges share a remarkably similar architecture. Furthermore, Afp12 can be regarded as a hybrid between gp7 and one of the gp6 copies, whereas the second gp6 is mimicked by Afp11. Indeed, alignment of Afp9 and gp25 overlays Afp11 and Afp12 with (gp6)$_2$-gp7 (Supplementary Fig. 9d). This structural conservation, unexpected from sequence analysis, highlights the importance of the Afp11-Afp12 (eq. (gp6)$_2$-gp7) module in the assembly and function of the baseplate. Close to the particle axis, Afp11 folds back to loosely bind the Afp8 needle just above the ß-helix. Because of the C3-symmetry of the latter, three copies of Afp11 interact with Afp8 more tightly than the other three (Fig. 5c). This fold back-interaction is different from those observed in T4[20], and mostly polar. The disorder observed in this region of Afp11 may facilitate needle ejection upon contraction. Situated at the periphery of the baseplate, Afp12 hosts the proximal end of the Afp13 tail fibre, which can be visualised in the local resolution filtered maps and upon varying the threshold (Supplementary Fig. 3b, e). As proposed for T4[20], recognition of receptors on the target cell surface may trigger rotation of the wedge and the fibres thereby initiating contraction.

Discussion

Although only 16 kDa in size, the sheath initiator protein Afp9 (eq. gp25) acts as a stabiliser and multivalent connector protein and appears to be crucial for assembly and structural integrity of the whole AFP particle. It is located at the inwards-pointing apex of the baseplate wedge and links the helical trunk to the Afp11-Afp12 bulk of the baseplate. Specifically, in the extended state, while the inner face of the Afp9 ring surrounds the tube initiator Afp7 and reaches to Afp5, its outer top side positions the first sheath ring formed by Afp4, and its lower external loops hold six Afp11-Afp12 modules in place (Fig. 5a, e). Comparison between the structures of the extended and contracted states reveals the crucial role of Afp9 as a power stroke initiator. Indeed, when the Afp13 fibres transmit the contraction signal through Afp12 to the rest of the wedge, the Afp11-Afp12 module detaches from the needle and swings outwards (Fig. 5d, Supplementary Fig. 9a, b). This momentum is transmitted to Afp9 which, in the contracted state, ensures the main connection between the baseplate wedge and the sheath (Fig. 5d, f). The exact sequence of

events and the cause-and-effect relationships require further investigation, but examination of the protein interaction networks inside the structures leads us to speculate that the swinging motion of the Afp9 connector with the whole of the wedge may transfer the contraction signal to Afp4 via two routes. The C-terminal α-helix of Afp9 would act as a hook pulling on the adjacent α-helix of Afp4 thereby causing rotation of the Afp4 subunit and its detachment from the tube Afp5. In addition, because Afp9 is the sheath initiator and the receiver of the first handshake from Afp4, its reorientation and the resulting movement of Afp4 would activate the transmission belt of handshakes that would spread from Afp4 to Afp2 and further up to the Afp16 cap. This would in turn trigger the sheath contraction, leading to the release of the tube and the needle, perforation of the target membrane and injection of the toxin into its grass grub prey.

In conclusion, this work presents the atomic resolution structures of an entire contractile injection nanomachine in both the extended and contracted states. It provides a molecular basis for understanding the PLTS mode of biological action and regulation, illustrates the degree of the universal conservation of CIS and offers a framework for their analysis with unprecedented detail. In addition, information offered by the AFP structures may be further used for biomedical design. One such example would be the rational modification of the AFP particle and its attachment fibres towards targeting specific mammalian cell surfaces for injection of a tailored biocontrol agent.

Methods

AFP expression and purification

Recombinant AFP was obtained as previously described[13]. Purified AFP sample was stored at 4°C in TM buffer (20mM Tris-HCl, 20 mM $MgCl_2$, pH 7.4). Contracted AFP was generated by incubating purified AFP samples with Gu-HCl at a final concentration of 3M for 1 minute at room temperature, then diluted in a large volume of TM buffer to stop the Gu-HCl action. Samples were then concentrated by ultracentrifugation for 1.5 hours at 150,000g and the pellet was resuspended in TM buffer. Cryo-EM specimens were then prepared immediately (see below).

Mass spectrometry

Briefly, protein samples were resolved by SDS-PAGE and bands were excised, destained, reduced with DTT, alkylated with iodoacetamide, then digested with sequencing grade porcine trypsin (Promega, Madison, WI, USA) in a chilled microwave (CEM, Matthews, NC, USA) at 45°C for 1 hour at 15 W. A 10 μl aliquot of each acidified digest was desalted on a 0.3 x 10 mm trap column packed with 3 μm Reprosil C18 media (Dr Maisch). Peptides were then separated on a 0.075x200 mm picofrit column (New Objective) packed in-house with 3 μm Reprosil C18 media using the following gradient of 0.1% formic acid in water (A) and 0.1% formic acid in acetonitrile (B) at 300 nl/min: 0 min 5% B, 0.5 min 5% B, 47 min 30% B, 49 min 98% B, 52 min 98% B, 53 min 5% B, 60 min 5% B. The picofrit spray was directed into a TripleTOF 6600 Quadrupole-Time-of-Flight mass spectrometer (Sciex, Framingham, MA, USA) operating in positive ion mode, scanning from m/z 350-1200 for

250ms, followed by up to forty 40 ms MS/MS scans per cycle (m/z 80-1600) on multiply-charged species using Dynamic Collision Energy and Dynamic Accumulation.

The resulting MS/MS data was then searched against an in-house protein sequence database containing selected entries from *Serratia entomophila* using ProteinPilot v5 (Sciex). Undetected proteins are indicated in Supplementary Table 1. Relative amounts of each detected protein were estimated using the total intensity of peptides corresponding to each protein, divided by the number of peptides expected upon trypsin digestion, after cleaning the raw results by confidence limit (> 80%), dmass (>0.03) and peptide MW (1000 Da < MW < 3300 Da). The relative numbers obtained were then normalised by considering the stoichiometry of Afp4 to be exactly 6 per AFP particle. This semi-quantification yielded relatively precise results, consistent with the cryo-EM map, in particular for proteins with large number of expected peptides, such as Afp11 (estimated at 6.1 copies per AFP particle) and Afp12 (estimated at 5.09 copies per AFP particle). According to this quantification, only one Afp18 toxin molecule (estimated at 0.97 copies) would be present per AFP particle.

Cryo-EM sample preparation

Cryo specimens were prepared using a Vitrobot (Mark IV) device. Typically 2-3 μl of a purified AFP sample was applied on a R2/2 Quantifoil grid (Pro Sci Tec) freshly glow-discharged in an amyl amine environment, blotted for 3 seconds and vitrified using a Vitrobot (Thermofisher) kept at 4°C and 100% humidity.

Cryo-EM data collection

Cryo-EM images of extended AFP were collected at EMBL Heidelberg, Germany, on a Titan Krios operated at 300 kV by Wim Hagen, with a condenser and objective lens apertures size of 50 μm, a spotsize of 8 and a beam diameter of 1.18 μm. In total, 5153 movies of 20 frames were acquired on a K2 camera in counting mode, with a dose rate of 2.5 e-/Å^2/s, a total exposure time of 8 s using 0.4 s frames, corresponding to 1 e-/Å^2 per frame and a total dose of 20 e-/Å^2. The calibrated pixel size at the specimen level was 1.35 Å at a nominal magnification of 37,000x.

Cryo-EM images of contracted AFP were collected at Korea Basic Science Institute Ochang Center, Republic of Korea, by Jaekyung Hyun, on a Titan Krios operated at 300kV, equipped with a Cs corrector (measured Cs of 500 nm after correction), using condenser and objective lens aperture size of 70 μm and 100 μm, respectively, a spotsize of 3 and a beam diameter of 850 nm. In total, 2847 movies of 30 frames were acquired on a Falcon II camera, with a dose rate of 35 e-/Å^2/s, a total exposure time of 1.8 s using 0.06 s frames, corresponding to ~2.1 e-/Å^2 per frame and a total dose of 63 e-/Å^2. The calibrated pixel size at the specimen level was 1.397 Å at a nominal magnification of 47,000x. A summary of cryo-EM data collection and processing (see below) parameters can be found in Supplementary Table 2.

Movie alignment, general processing strategy, particle picking and defocus estimation

For both datasets, the frames alignment was done with IMOD alignframes[41], keeping frames 2-20 (total dose 20e-/Å^2) for extended AFP, and frames 2-13 (total dose 27e-/Å^2) for contracted AFP. Extended AFP particles were divided into three independently processed

parts – the baseplate, the trunk and the cap (Supplementary Fig. 1). To this end, the precise coordinates of the extremities (from the largest baseplate width to the apex of the cap) of 30858 particles were manually recorded using EMAN2's e2helixboxer.py[42], corresponding to a total particle length of 3.19 mm. In order to use baseplates from particles with overlapping trunks or caps or extended outside the field of view, additional 16133 baseplates were manually selected with e2helixboxer.py, corresponding to a total number of 46991 baseplates (Supplementary Fig. 1).

For contracted AFP, a 3D reconstruction without helical symmetry imposition was calculated from one central segment per contracted particle. Helical parameters of this initial map were determined (see below) and a final structure calculated using overlapping segments and taking the helical symmetry into account. For this purpose, the precise coordinates of the extremities of 15189 particles were manually recorded using e2helixboxer.py, corresponding to a total particle length of 0.63 mm. Details of optimised segment extraction are summarised in Supplementary Figures 1 and 2. Helical segmentation for the contracted sheath was performed using SPRING[43]. The defocus estimation was done with CTFFIND3/CTFTILT[44] or with CTFFIND4[43]. For symmetry refinement, phase flipped segments were extracted, whereas for high-resolution 3D reconstruction convolved segments were used. For all 3D refinements, the search in out-of-plane tilt was limited to 12°. Figures were prepared using Chimera and ChimeraX[45,46].

Extended AFP – Trunk

Analogously to all known CIS structures, the trunk of the extended AFP particle can be considered as an assembly of six protofilaments forming a right-handed superhelix (Fig. 2a)[47]. Alternatively, one can adopt a historical description and define the inner tube as tightly stacked hexameric rings or layers, related to each other by a 20.14° rotation and a 39.32 Å translation along the particle axis, which is a helical symmetry similar to the other CIS[47]. Due to Afp2/Afp3 alternation, the helical geometry of the sheath is described by a rise of 78.64 Å and a rotation of 40.28°, exactly twice that of the enclosed tube of Afp1. To determine this symmetry, refinement was performed using the previous 20 Å resolution reconstruction of the AFP trunk[13] as an initial model, with 20 cycles of IHRSR[48] refinement implemented in Spider[49,50], wherein the helical rise was varied from 78 to 81 Å in 1.5 Å steps and the rotation between subunits varied from 40.5 to 42.5° in 1° steps (Supplementary Fig. 1). For each initial symmetry choice, the symmetry parameters were refined with the hsearch[48] program using step sizes of 0.1 Å for the helical rise and 0.1° for the azimuthal rotation, for the iterations 2-13. For cycles 14-20, the steps were decreased to 0.05 Å and 0.05° respectively, and a finer increment was used to project the reference volume. The average final values of 78.57 Å for the rise and 40.15° for the helical rotation were then used for high resolution refinement in SPRING, which yielded a reconstruction of the trunk at an overall estimated resolution of 2.9 Å at FSC cut-off 0.143 and with an automatically determined b-factor of -105 Å^{-2}. Per particle CTF determination with Gctf[51] and helical auto-refine procedure as implemented in RELION-3[52] (with symmetry refinement), further improved the map, resulting in the final reconstruction at an overall resolution of 2.78 Å (FSC at 0.143 cut-off) and with an automatically determined b-factor of -92 Å^{-2}, obtained

from 122721 segments (after removal of outplane outliers) corresponding to 736326 asymmetric units after C6 symmetrisation.

Contracted AFP – Sheath

Using a hollow cylinder of 70 Å inner diameter and 230 Å outer diameter as an initial model, a 3D refinement in RELION-2.1[53], imposing only C6 symmetry, resulted in map with 4.2 Å resolution after automatic masking (FSC cut-off 0.143). This map was then used to determine the helical symmetry as follows. Based on a first visual inspection of this C6-symmetrised map, helical rise between 30 and 36 Å (0.2 Å steps) and azimuthal rotation between 2 to 5° (0.1° steps) were tested by imposing each symmetry with the program himpose[48] and recording the variance of each symmetrised reconstruction. A finer search around the parameters corresponding to the highest variance (*i.e.* reinforcement of features) was then performed with the rise ranging from 34.8 to 35.2 Å (0.02 Å steps) and the rotation ranging from 3 to 3.2 ° (0.01° step) (Supplementary Fig. 2). The resulting best symmetry of 34.97 Å helical rise and 3.14° azimuthal rotation was then used for further processing in SPRING. High resolution 3D refinement gave a final map at an overall resolution of 3.8 Å (FSC at 0.143 cut-off) (Supplementary Fig. 4), obtained from 46022 segments corresponding to 276132 asymmetric units after helical and C6 symmetrisation. For model building and figures, this map was filtered at 3.8 Å and sharpened with a bfactor of -260 Å^{-2}.

Contracted AFP – Baseplate

Extremities with and without contracted baseplate were sorted by 2D classification (Supplementary Fig. 2). The C6-symmetrised reconstruction of the entire contracted trunk was shifted and masked to match the position of extracted extremities, and used as initial reference for a RELION-2.1 auto-refine procedure using C6 symmetry. The resulting map, with an average of 4.6 Å resolution (FSC at 0.143 cut-off) showed poorly resolved baseplate region. Masked 3D classification of this region with no further alignment enabled to group the particles by their baseplate conformation (more or less open). A final auto-refine of each group led to three contracted baseplate maps with an overall resolution of 5.4, 5.9 and 7.3 Å. The best map was used for refining the models of proximal Afp2 and Afp4, and placing Afp9,11 and 12 as rigid bodies in the lower resolution baseplate wedge density.

Extended AFP – Baseplate

The previously published 20 Å AFP reconstruction[13] was appropriately masked to enclose the baseplate part, and used as initial reference for a RELION-2.1 auto-refine procedure using C6 symmetry. This gave a reconstruction with a resolution of 3.2 Å (FSC at 0.143 cut-off after automatic masking, 3.6 Å without masking). To further improve the resolution, alignment and resolution dependent-weighting of the individual particle movie frames (particle polishing), were performed in RELION-2.1, using all the frames and a running average of 5 frames during movie expansion. Final refinement using these polished particles resulted in a reconstruction with an overall resolution of 3.1 Å (FSC at 0.143 cut-off after automatic masking, 3.5 Å without masking), and with a determined overall b-factor of -105 Å^{-2}.

Extended AFP – Needle

The C6-symmetrised baseplate reconstruction did not allow to resolve the needle, suggesting that, as in other related CIS, this region may have a 3-fold symmetry. However, attempts of baseplate reconstruction with C3 symmetry imposed did not lead to improvement. Furthermore, due to the relative low mass of the needle region in comparison to the rest of the baseplate, 3D classification of aligned particles (skipping alignment) in two classes was inefficient. Therefore, the localised reconstruction approach[54] was used (Supplementary Fig. 1). The contribution of all the baseplate except the needle region and close surroundings was subtracted from the raw particles using relion_localized_reconstruction.py, according to the orientations corresponding to the best map of the baseplate before particle polishing, and sub-particles were newly boxed with a size of 180x180 pixels around the defined centre of the needle. Using these orientations, a 3D reconstruction of the subtracted particles was generated with relion_reconstruct, in order to obtain an initial model of the needle. Subsequently, 3D classification without alignment and using C3 symmetry resulted in a separation of the subtracted particles into two classes, each corresponding to a possible orientation of the C3 symmetric needle relative to the C6 symmetric baseplate. Based on this 3D classification, a rotation of 60° around z was applied to the particles corresponding to one class by modifying the orientations parameter file. Using these modified orientations, a first correct C3 reconstruction of the needle was computed from the subtracted particles, and a solvent mask surrounding the needle region was created. These were used as inputs for further refinement of orientations using local searches only. This workflow lead to a final C3-symmetrised map from the subtracted particles with an overall resolution of 3.7 Å (FSC at 0.143 cut-off). Inspection of this map revealed a poorly resolved upper region of the needle, where significant overlap with the rest of the baseplate's projection would occur in the side views, suggesting artefacts due to the signal subtraction itself (Supplementary Fig. 1). Therefore, orientations of the subtracted images refined with a C3 symmetry were applied to the original non-subtracted baseplate particles, and a final local orientation refinement was performed with the C3 symmetry imposed. This gave a 3-fold symmetric map of the entire baseplate with no artefacts in the upper region of the needle and with an overall resolution of 3.3 Å (FSC at 0.143 cut-off after automatic masking, 3.8 Å without masking), and with an automatically determined overall bfactor of -102 Å^{-2}.

Extended AFP – Cap

The 20 Å AFP reconstruction[13] was appropriately masked to enclose the cap region, and used as initial reference for a RELION-2.1 auto-refine procedure using C6 symmetry. This gave a reconstruction with an overall resolution of 3.4 Å without masking, but with a poor definition of the cap end, and with sheath protrusions appearing at every sheath layer instead of every two layers (Supplementary Fig. 1). Using the orientations corresponding to this map, 3D classification into two classes (skipping alignment) showed that the terminal sheath ring was built either by Afp2 or Afp3. The particles from both "Afp2-terminating" and "Afp3-terminating" classes were further subjected to 3D classification into 3 classes each, still without alignment. One class of "Afp2-terminating" particles corresponded to a ~40 Å (distance between Afp2 and Afp3 rings in the sheath) shifted map, ending with Afp3. This can be explained by the fact that the alignment in the first refinement was driven by the helical sheath region, disregarding the cap region due to its much lower mass. Similarly, two

classes from the "Afp3-terminating" particles were shifted by 40 Å, down and up the helical axis, and corresponded to the actual Afp2-terminating particles. According to this result, the particles were newly grouped by sheath-terminating protein, and used for 3D refinement with a larger translational search. Two additional rounds of 3D classification and re-grouping of particles according to the terminal sheath protein were performed, resulting in the separation of the dataset into 23797 Afp2-terminating particles (77% of all particles) and 7061 Afp3-terminating particles (23% of all particles). Finally, a 3D refinement of each dataset with alignment parameter search and with the final 3D classes as references led to reconstructions of the cap with an overall resolution of 3.2 and 3.4 Å (FSC at 0.143 cut-off after automatic masking, 3.5 and 3.8 Å without masking) and with a determined overall bfactor of -102 Å^{-2} or -82 Å^{-2} for the maps with the terminal Afp2-Afp16 and Afp3-Afp16 interaction, respectively. To assess the resolution of the cap part only, a tighter mask enclosing this region was created and combined with the automatic mask calculated by relion_postprocess, and the cap resolution was estimated to be 3.3 and 3.4 Å for the terminal Afp2-Afp16 map and the terminal Afp3-Afp16 map, respectively (FSC at 0.143 cut-off).

For each map, the local resolution was calculated using relion_postprocess except for the helical contracted sheath for which ResMap[55] was used.

Merging maps into chimeric full extended AFP structure

The entire AFP map shown in Fig. 1 was assembled from the following post-processed maps scaled by a factor of 2, after appropriate masking to exclude overlaps and gaps, and applying translation and rotation: Afp2-Afp16 terminating extended AFP cap, helical trunk (SPRING reconstruction), 6-fold symmetric baseplate (needle region removed) and 3-fold symmetric baseplate (needle region only). This map was subsequently downscaled to the original pixel size, and filtered to 3.2Å.

Model building and refinement

Atomic models were built into their respective cryo-EM maps *ab initio*, by first manually tracing each protein sequence into the maps using Coot[56], and further refined using phenix.real_space_refine[57] implemented in the rsref refinement pipeline[58], using each map's local resolution as a target. Several iterations of automatic real space refinement followed by manual adjustments in Coot were performed until convergence. Symmetry-related copies and neighbouring subunits were taken into account by including all subunits present in each map during final refinements. For Afp11 and Afp12, which had regions with poorer resolved densities, LocScale[59] was used to apply local sharpening on the baseplate map for final steps of refinements. For Afp11 and Afp12, manual building in Coot was followed by a single round of molecular dynamics flexible fitting using NAMDINATOR[60], and by a final round of real space refinement in Phenix. A summary of model refinement and validation statistics can be found in Supplementary Table 3.

Interaction energy calculations

Interaction energies between AFP subunits were performed using the PISA server[61]. After performing PISA calculations, -0.5 kcal/mol per hydrogen bond and -0.3 kcal/mol per salt bridge were added to the free energy determined by PISA (Supplementary Tables 4-6).

Supplementary Material

Refer to Web version on PubMed Central for supplementary material.

Acknowledgements

Data availability

Cryo-EM maps and corresponding atomic coordinates have been deposited to the EMDB and PDB with accession codes: full extended AFP composite map (EMD-4783), extended AFP baseplate C6 map (EMD-4782, 6RAO), extended AFP baseplate C3 map (EMD-4800, 6RBK), extended AFP cap ending in Afp2-Afp16 (EMD-4784, 6RAP), extended AFP cap ending in Afp3-Afp16 (EMD-4801), extended AFP sheath map (EMD-4802, 6RBN), extended AFP needle map from subtracted images (EMD-4871), contracted AFP sheath map (EMD-4803, 6RC8), contracted AFP baseplate (EMD-4876, 6RGL), contracted AFP sheath C6 map (EMD-4859). All other data supporting the findings of this study are available from AD and IG upon request.

References

1. Kube S, Wendler P. Structural comparison of contractile nanomachines. AIMS Biophys. 2015; 2:88–115.

2. Taylor NMI, van Raaij MJ, Leiman PG. Contractile injection systems of bacteriophages and related systems. Mol Microbiol. 2018; 108:6–15. [PubMed: 29405518]

3. Patz S, et al. Phage tail-like particles are versatile bacterial nanomachines – A mini-review. J Adv Res. 2019

4. Leiman PG, et al. Type VI secretion apparatus and phage tail-associated protein complexes share a common evolutionary origin. Proc Natl Acad Sci U S A. 2009; 106:4154–9. [PubMed: 19251641]

5. Brackmann M, Nazarov S, Wang J, Basler M. Using Force to Punch Holes: Mechanics of Contractile Nanomachines. Trends Cell Biol. 2017; 27:623–632. [PubMed: 28602424]

6. Nguyen VS, et al. Towards a complete structural deciphering of Type VI secretion system. Curr Opin Struct Biol. 2018; 49:77–84. [PubMed: 29414515]

7. Nakayama K, et al. The R-type pyocin of Pseudomonas aeruginosa is related to P2 phage, and the F-type is related to lambda phage. Mol Microbiol. 2000; 38:213–31. [PubMed: 11069649]

8. Michel-Briand Y, Baysse C. The pyocins of Pseudomonas aeruginosa. Biochimie. 2002; 84:499–510. [PubMed: 12423794]

9. Ge P, et al. Atomic structures of a bactericidal contractile nanotube in its pre- and postcontraction states. Nat Struct Mol Biol. 2015; 22:377–382. [PubMed: 25822993]

10. Hurst MRH, Glare TR, Jackson TA. Cloning Serratia entomophila antifeeding genes--a putative defective prophage active against the grass grub Costelytra zealandica. J Bacteriol. 2004; 186:5116–28. [PubMed: 15262948]

11. Yang G, Dowling AJ, Gerike U, Ffrench-Constant RH, Waterfield NR. Photorhabdus virulence cassettes confer injectable insecticidal activity against the wax moth. J Bacteriol. 2006; 188:2254–2261. [PubMed: 16513755]

12. Sarris PF, Ladoukakis ED, Panopoulos NJ, Scoulica EV. A phage tail-derived element withwide distribution among both prokaryotic domains: A comparative genomic and phylogenetic study. Genome Biol Evol. 2014; 6:1739–1747. [PubMed: 25015235]

13. Heymann JB, et al. Three-dimensional structure of the toxin-delivery particle antifeeding prophage of serratia entomophila. J Biol Chem. 2013; 288:25276–25284. [PubMed: 23857636]

14. Jiang F, et al. Cryo-EM Structure and Assembly of an Extracellular Contractile Injection System. Cell. 2019; :1–14. DOI: 10.1016/j.cell.2019.02.020

15. Shikuma NJ, et al. Marine Tubeworm Metamorphosis Induced by Arrays of Bacterial. Science. 2014; 343:529–534. [PubMed: 24407482]

16. Böck D, et al. In situ architecture, function, and evolution of a contractile injection system. Science (80-.). 2017; 357:713–717.

17. Kudryashev M, et al. Structure of the Type VI secretion system contractile sheath. Cell. 2015; 160:952–962. [PubMed: 25723169]

18. Wang J, et al. Cryo-EM structure of the extended type VI secretion system sheath-tube complex. Nat Microbiol. 2017; 2:1507–1512. [PubMed: 28947741]

19. Nazarov S, et al. Cryo-EM reconstruction of Type VI secretion system baseplate and sheath distal end. EMBO J. 2017; 37:e97103. [PubMed: 29255010]

20. Taylor NMI, et al. Structure of the T4 baseplate and its function in triggering sheath contraction. Nature. 2016; 533:346–352. [PubMed: 27193680]

21. Hurst MR, Glare TR, Jackson TA, Ronson CW. Plasmid-located pathogenicity determinants of Serratia entomophila, the causal agent of amber disease of grass grub, show similarity to the insecticidal toxins of Photorhabdus luminescens. J Bacteriol. 2000; 182:5127–38. [PubMed: 10960097]

22. Rybakova D, et al. Role of antifeeding prophage (Afp) protein Afp16 in terminating the length of the Afp tailocin and stabilizing its sheath. Mol Microbiol. 2013; 89:702–714. [PubMed: 23796263]

23. Rybakova D, Schramm P, Mitra AK, Hurst MRH. Afp14 is involved in regulating the length of Anti-feeding prophage (Afp). Mol Microbiol. 2015; 96:815–826. [PubMed: 25689688]

24. Hurst MRH, et al. Serratia proteamaculans Strain AGR96X Encodes an Antifeeding Prophage (Tailocin) with Activity against Grass Grub (Costelytra giveni) and Manuka Beetle (Pyronota Species) Larvae. Appl Environ Microbiol. 2018; 84

25. Pell LG, Kanelis V, Donaldson LW, Howell PL, Davidson AR. The phage lambda major tail protein structure reveals a common evolution for long-tailed phages and the type VI bacterial secretion system. Proc Natl Acad Sci U S A. 2009; 106:4160–5. [PubMed: 19251647]

26. Arnaud C-A, et al. Bacteriophage T5 tail tube structure suggests a trigger mechanism for Siphoviridae DNA ejection. Nat Commun. 2017; 8:1953. [PubMed: 29209037]

27. Biggs DR, McGregor PG. Gut pH and amylase and protease activity in larvae of the New Zealand grass grub (Costelytra zealandica; Coleoptera: Scarabiaedae) as a basis for selection inhibitors. Insect Biochem Mol Biol. 1996; 26:69–75.

28. Bateman A, Bycroft M. The structure of a LysM domain from E. coli membrane-bound lytic murein transglycosylase D (MltD). J Mol Biol. 2000; 299:1113–9. [PubMed: 10843862]

29. Wang J, et al. Cryo-EM structure of the extended type VI secretion system sheath-tube complex. Nat Microbiol. 2017; 2:1507–1512. [PubMed: 28947741]

30. Zheng W, et al. Refined Cryo-EM Structure of the T4 Tail Tube: Exploring the Lowest Dose Limit. Structure. 2017; 25:1436–1441.e2. [PubMed: 28757144]

31. Bönemann G, Pietrosiuk A, Diemand A, Zentgraf H, Mogk A. Remodelling of VipA/VipB tubules by ClpV-mediated threading is crucial for type VI protein secretion. EMBO J. 2009; 28:315–25. [PubMed: 19131969]

32. Zoued A, et al. Priming and polymerization of a bacterial contractile tail structure. Nature. 2016; 531:59–63. [PubMed: 26909579]

33. Zoued A, et al. TssA: The cap protein of the Type VI secretion system tail. Bioessays. 2017; 39

34. Fokine A, et al. The molecular architecture of the bacteriophage T4 neck. J Mol Biol. 2013; 425:1731–44. [PubMed: 23434847]

35. Pell LG, et al. The X-ray crystal structure of the phage lambda tail terminator protein reveals the biologically relevant hexameric ring structure and demonstrates a conserved mechanism of tail termination among diverse long-tailed phages. J Mol Biol. 2009; 389:938–51. [PubMed: 19426744]

36. Cherrak Y, et al. Biogenesis and structure of a type VI secretion baseplate. Nat Microbiol. 2018; 3:1404–1416. [PubMed: 30323254]

37. Park Y-J, et al. Structure of the type VI secretion system TssK-TssF-TssG baseplate subcomplex revealed by cryo-electron microscopy. Nat Commun. 2018; 9:5385. [PubMed: 30568167]

38. Shneider MM, et al. PAAR-repeat proteins sharpen and diversify the type VI secretion system spike. Nature. 2013; 500:350–353. [PubMed: 23925114]

39. Kanamaru S, Ishiwata Y, Suzuki T, Rossmann MG, Arisaka F. Control of bacteriophage T4 tail lysozyme activity during the infection process. J Mol Biol. 2005; 346:1013–20. [PubMed: 15701513]

40. Quentin D, et al. Mechanism of loading and translocation of type VI secretion system effector Tse6. Nat Microbiol. 2018; 3:1142–1152. [PubMed: 30177742]

41. Kremer JR, Mastronarde DN, McIntosh JR. Computer visualization of three-dimensional image data using IMOD. J Struct Biol. 1996; 116:71–6. [PubMed: 8742726]

42. Tang G, et al. EMAN2: an extensible image processing suite for electron microscopy. J Struct Biol. 2007; 157:38–46. [PubMed: 16859925]

43. Rohou A, Grigorieff N. CTFFIND4: Fast and accurate defocus estimation from electron micrographs. J Struct Biol. 2015; 192:216–21. [PubMed: 26278980]

44. Mindell JA, Grigorieff N. Accurate determination of local defocus and specimen tilt in electron microscopy. J Struct Biol. 2003; 142:334–47. [PubMed: 12781660]

45. Pettersen EF, et al. UCSF Chimera--a visualization system for exploratory research and analysis. J Comput Chem. 2004; 25:1605–12. [PubMed: 15264254]

46. Goddard TD, et al. UCSF ChimeraX: Meeting modern challenges in visualization and analysis. Protein Sci. 2018; 27:14–25. [PubMed: 28710774]

47. Kube S, Wendler P. Structural comparison of contractile nanomachines. AIMS Biophys. 2015; 2:88–115.

48. Egelman EH. A robust algorithm for the reconstruction of helical filaments using single-particle methods. Ultramicroscopy. 2000; 85:225–34. [PubMed: 11125866]

49. Frank J, et al. SPIDER and WEB: processing and visualization of images in 3D electron microscopy and related fields. J Struct Biol. 1996; 116:190–9. [PubMed: 8742743]

50. Shaikh TR, et al. SPIDER image processing for single-particle reconstruction of biological macromolecules from electron micrographs. Nat Protoc. 2008; 3:1941–74. [PubMed: 19180078]

51. Zhang K. Gctf: Real-time CTF determination and correction. J Struct Biol. 2016; 193:1–12. [PubMed: 26592709]

52. Zivanov J, et al. New tools for automated high-resolution cryo-EM structure determination in RELION-3. Elife. 2018; 7

53. Scheres SHW. RELION: implementation of a Bayesian approach to cryo-EM structure determination. J Struct Biol. 2012; 180:519–30. [PubMed: 23000701]

54. Ilca SL, et al. Localized reconstruction of subunits from electron cryomicroscopy images of macromolecular complexes. Nat Commun. 2015; 6

55. Kucukelbir A, Sigworth FJ, Tagare HD. Quantifying the local resolution of cryo-EM density maps. Nat Methods. 2014; 11:63–5. [PubMed: 24213166]

56. Emsley P, Lohkamp B, Scott WG, Cowtan K. Features and development of Coot. Acta Crystallogr D Biol Crystallogr. 2010; 66:486–501. [PubMed: 20383002]

57. Adams PD, et al. PHENIX: a comprehensive Python-based system for macromolecular structure solution. Acta Crystallogr D Biol Crystallogr. 2010; 66:213–21. [PubMed: 20124702]

58. Hoffmann NA, Jakobi AJ, Vorländer MK, Sachse C, Müller CW. Transcribing RNA polymerase III observed by electron cryomicroscopy. FEBS J. 2016; 283:2811–9. [PubMed: 27059519]

59. Jakobi AJ, Wilmanns M, Sachse C. Model-based local density sharpening of cryo-EM maps. Elife. 2017; 6

60. Kidmose RT, Nissen P, Boesen T, Karlsen JL, Pedersen BP. Namdinator - Automatic Molecular Dynamics flexible fitting of structural models into cryo-EM and crystallography experimental maps. bioRxiv. 2019; doi: 10.1101/501197

61. Krissinel E, Henrick K. Inference of macromolecular assemblies from crystalline state. J Mol Biol. 2007; 372:774–97. [PubMed: 17681537]
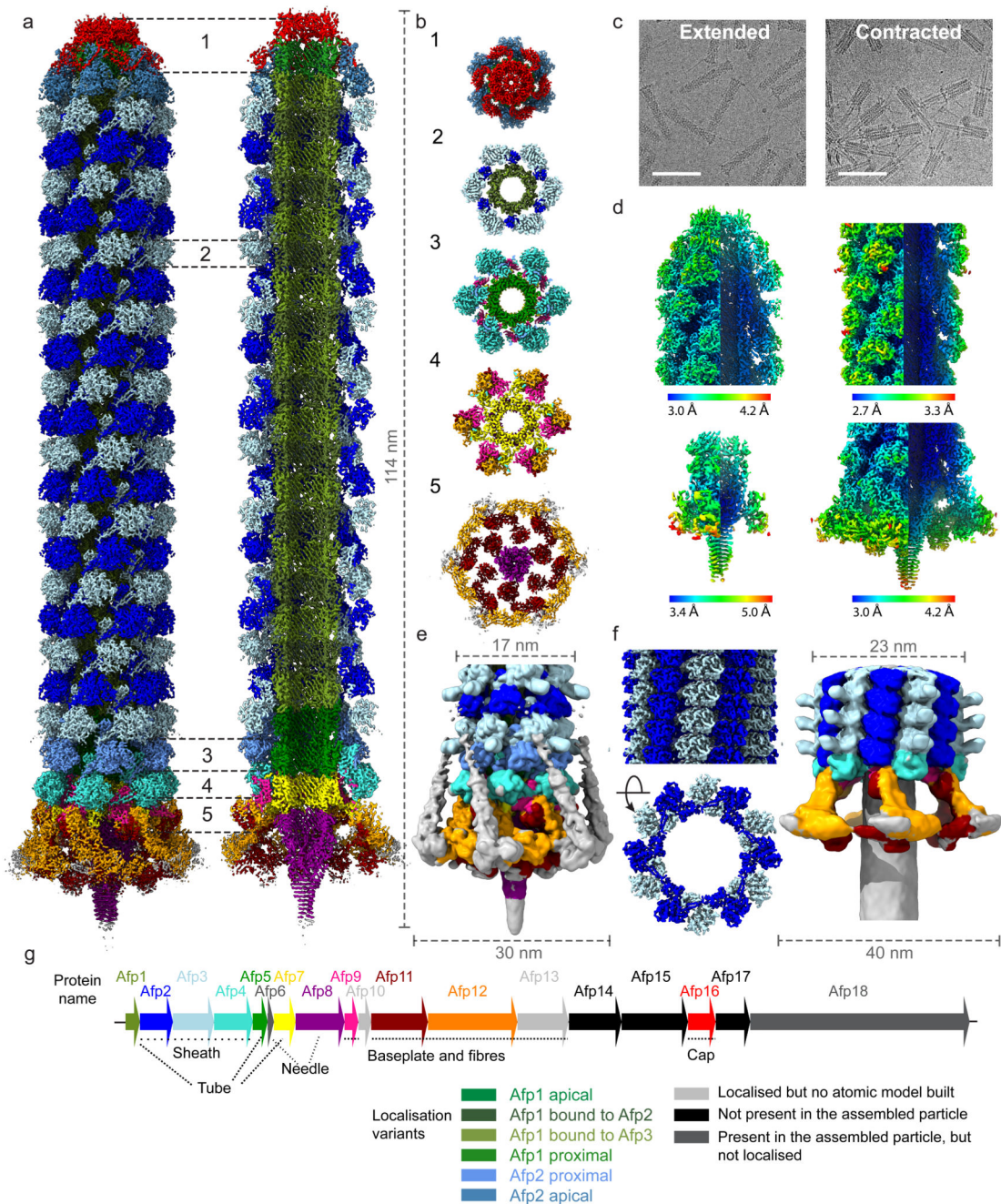
Figure 1. Cryo-EM structures of the complete antifeeding prophage (AFP) contractile injection system in extended and contracted states.

(a) Composite cryo-EM map, assembled from individual maps of the AFP cap, trunk, baseplate and needle, showing the overall organisation of AFP in the extended state. The map corresponds to the main population of AFP particles terminating in Afp2 below the apical cap. Different subunits are coloured according to panel g. (b) Cut-out view of different sections (1 – 5) labelled in panel a. (c) Representative micrographs displaying AFP particles in the extended (left) and contracted (right) state. The scale bars on both micrographs are 100 nm. (d) Cryo-EM maps for the apical end cap (upper left), the sheath

and tube (upper right), the needle (lower left) and the baseplate (lower right) coloured according to local resolution. (e) Cryo-EM map of AFP in the extended state, filtered to a resolution of 10 Å, allowing for a better visualisation of the Afp13 tail fibres and Afp3 protrusions. (f) Cryo-EM maps of the sheath (left) and baseplate (right) of AFP in the contracted state, with different subunits coloured according to panel g. The length and/or width (in nm) of maps shown in a, e and f is annotated using dashed lines. (g) Schematic representation of genomic organisation of the AFP gene cluster.

Figure 2. Molecular organisation of the AFP extended state inner tube.
(a) Cryo-EM map of the AFP extended state, displaying selected subunits involved in interactions within the inner tube, between the inner tube and sheath, and between the inner tube and apical cap. (b) Structural alignment between Afp1 in the inner tube (coloured olive green), Afp1 in the apical cap (dark green), Afp5 (light green) and Afp7 (yellow). Note the differences in conformation of the N-terminus of Afp1 in the apical cap (α-helical turn) and inner tube (unfolded). Insets display density for Afp5 built into the cryo-EM map of the AFP extended state trunk to illustrate that the Afp5 ring is the best-resolved baseplate component (2.9 Å resolution), with the structure featuring putative water molecules and a putative metal ion coordinated by three methionines (labelled in black). (c) Interaction between Afp16 (red) and Afp1 (green) in the apical cap. The loop of Afp16 which intercalates between the central

β-sheet of Afp1 is shown in light yellow. The N-terminus of Afp1 bound to the cap (Afp1 apical) is unfolded and interacts with Afp16. (d) Interactions between one copy of Afp1 contacting Afp3 (labelled 'Afp1 bound to Afp3', coloured olive green) in layer n, and four copies of Afp1 contacting Afp2 (labelled 'Afp1 bound to Afp2', coloured red to blue) in layer n-1 (bottom) and n+1 (top) in the inner tube. The N-terminus of Afp1 in layer n forms an α-helical turn and is coloured light blue. (e) Interaction between Afp5 (green) and Afp7 (yellow). The loop of Afp5 which intercalates between the central β-sheet of Afp7 is shown in light blue. The C-terminal domain of Afp7 (LysM domain) is labelled in black. (f) Interaction between two adjacent copies of Afp7, coloured yellow (ni) and orange (ni+1), and Afp8 (coloured purple). The loops the two Afp7 copies which intercalate between the central β-sheet of Afp8 are shown in two tints of light blue. (g) Structural alignment of LysM domains of Afp7 (yellow), Pvc7 (purple, PDB ID: 6J0N), gp53 (blue, PDB ID: 5IV5) and MltD (orange, PDB ID: 1E0G). (h) Zoom on the LysM domain of the structural alignment shown in (g).
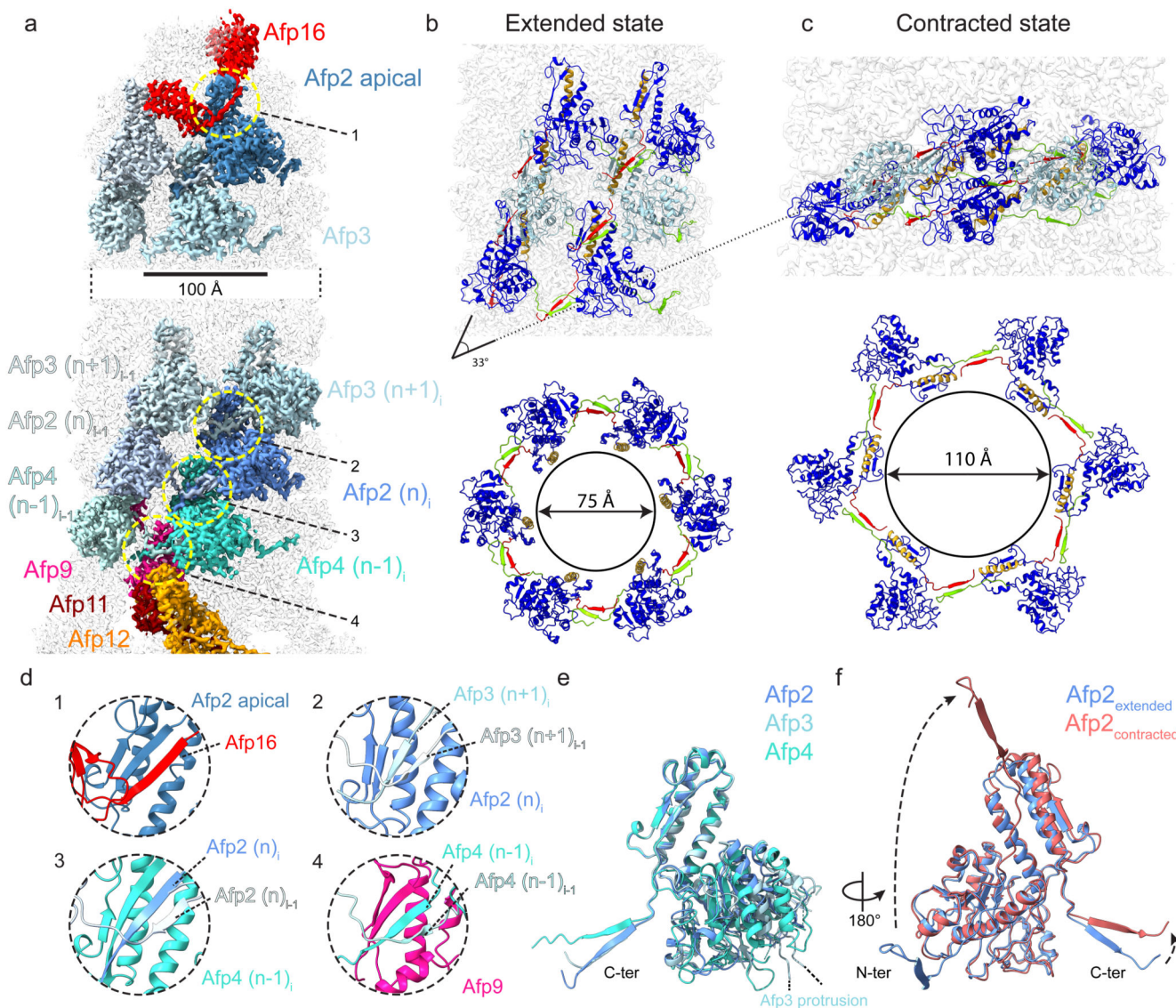
Figure 3. Molecular organisation of the AFP sheath in the extended and contracted state.
(a) Cryo-EM map of the AFP extended state, displaying selected subunits involved in interactions within the sheath, between the sheath and apical cap, and between the sheath and baseplate. (b-c) Molecular rearrangement of Afp2 (dark blue) and Afp3 (light blue) subunits in the sheath upon AFP contraction. The N- and C-termini of both Afp2 and Afp3 are coloured green and red respectively, while tube interacting helix (res. 277-297 for Afp2, res. 374-394 for Afp3) is coloured orange. The angle between alternating Afp2 and 3 subunits changes 33°, while the diameter of the sheath expands from 75 Å (extended state) to 110 Å (contracted state) (b and c). (d) Insets showing a zoom of the dotted yellow circles annotated in panel (a). The insets display different instances of a β-strand exchange (termed handshake mechanism) between Afp2 (dark blue) and Afp16 (red) in the apical cap (upper left), Afp2 (dark blue) and Afp3 (light blue and pale blue) in the sheath (upper right), Afp2 (dark blue) and Afp4 (cyan and light cyan) in the upper baseplate (lower left) and Afp4

(cyan and light cyan) and Afp9 (violet) in the lower baseplate (lower right). (e) Structural alignment between Afp2 (dark blue), Afp3 (light blue) and Afp4 (cyan). The location of the Afp3 protrusion (not modelled) is indicated with dashed lines. (f) Structural alignment between Afp2 in the extended (blue) and contracted (red) state. Note the large rearrangements of both N- and C-termini of Afp2 upon AFP contraction.
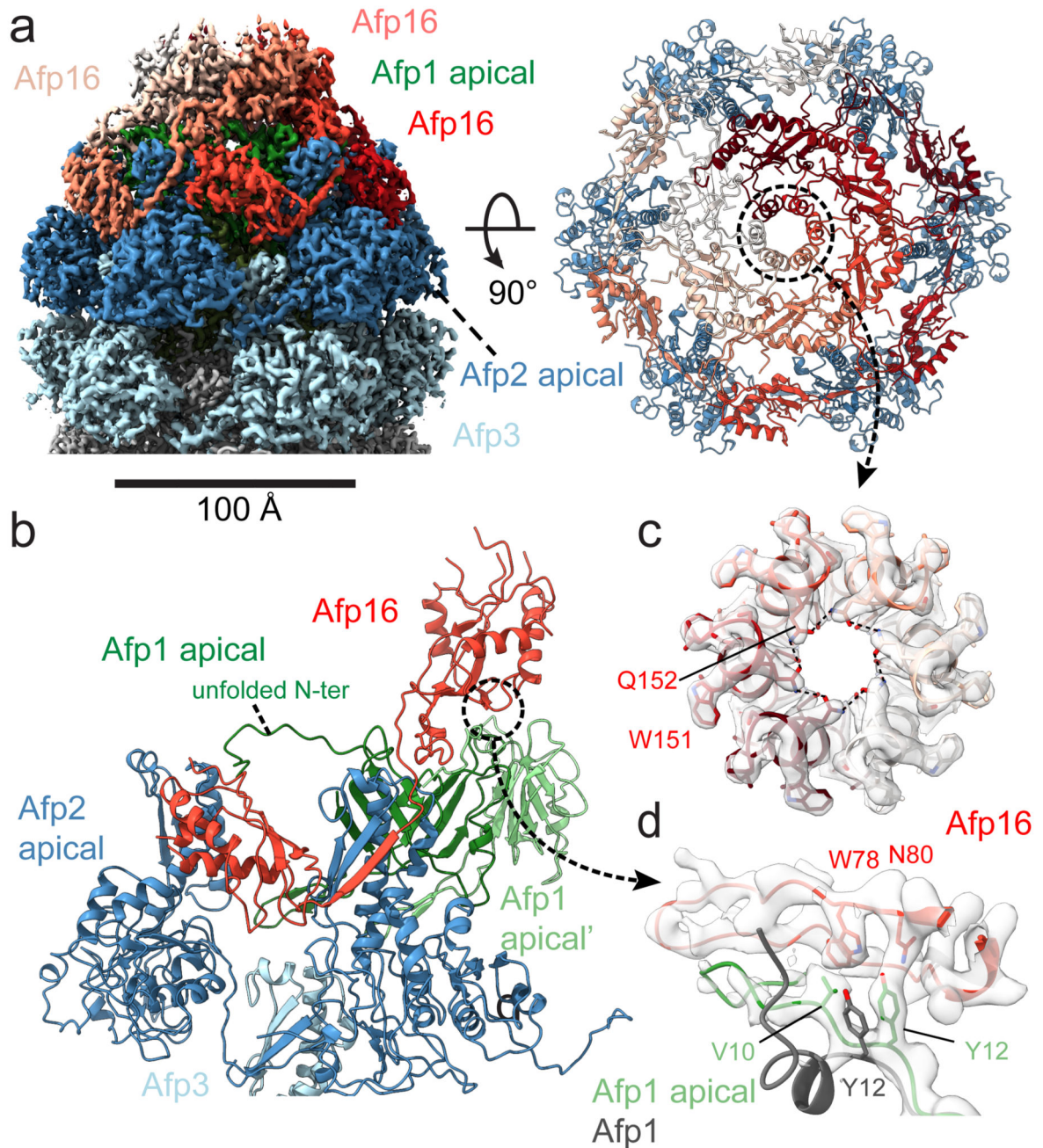
Figure 4. Architecture of the AFP extended state apical cap.
(a) Left: Cryo-EM map of the AFP extended state apical cap, displaying subunits Afp1 (green), Afp2 (dark blue), Afp3 (light blue), and Afp16 (light to dark red). Right: Top-view of fitted Afp2 (dark blue) and Afp16 (white to dark red) subunits. Note the central ring formed by a side-by-side stacking of the helix spanning residues 143 to 153 of neighbouring Afp16 subunits (annotated by a dotted black circle). (b) Interactions between Afp1 (light and dark green), Afp2 (dark blue), Afp3 (light blue) and Afp16 (red) in the apical cap. The linker ß-strand (res. 184-191) of Afp16 is involved in a handshake with Afp2. (c) Density of the

central ring in the apical cap with fitted α-helices containing residues 143 to 153 of neighbouring Afp16 subunits. Amino acids Glutamine 152 (Q152) and Tryptophan 151 (W151) are labelled and shown as sticks. (d) Density displaying the interaction between Afp16 (red) and the N-terminus of Afp1 in the apical cap (green). Amino acids Valine 10 (V10) and Tyrosine 12 (Y12) of Afp1, and tryptophan 78 (W78) and Asparagine 80 (N80) of Afp16 are labelled and shown as sticks. An alignment is shown of Afp1 in the sheath (grey) with Afp1 bound to the cap (green), to illustrate the rearrangements of N-terminal residues V10 and V12 upon Afp16 binding.
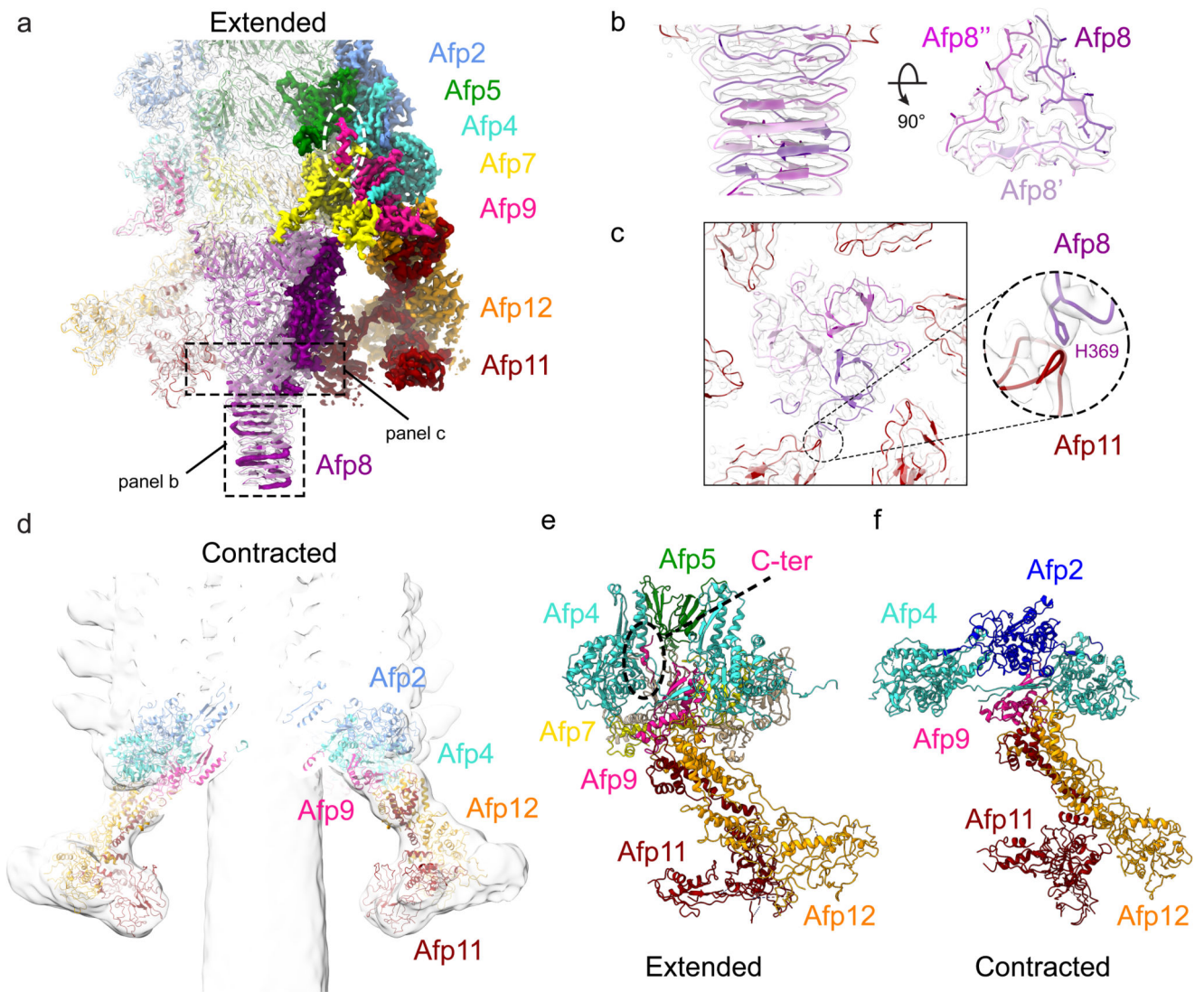
Figure 5. Molecular organisation of the AFP baseplate in the extended and contracted state.
(a) Cryo-EM map of the AFP baseplate in the extended state. Selected subunits involved in interactions between the tube, sheath and baseplate, and within the baseplate itself are displayed as non-transparent density, while transparent density contains structures of subunits Afp2, 4, 5, 7, 9, 11 and 12. (b) Density of the AFP needle formed by three neighbouring Afp8 subunits (coloured light to dark purple). Hydrophobic residues in the 3-fold symmetric centre of the needle tip are shown as sticks. (c) Pseudo-hexameric symmetry of the upper part of the AFP needle. Note the alternating presence/absence of interactions between residue Histidine 369 (H369) of Afp8 (purple) and a loop of Afp11 (dark red), indicating the transition between 6-fold to 3-fold symmetry in the AFP needle. (d) Cryo-EM map of the AFP baseplate in the contracted state. A fit is shown of subunits Afp2, Afp4, Afp9, Afp11 and Afp12 in the contracted baseplate map. (e-f) Comparison between structural organisation of the extended (e) and contracted (f) baseplate. Note the α-helical conformation of the C-terminus of Afp9 (violet) in the extended (e) AFP state (annotated

with a dotted black oval), while it is unstructured and thus not present in the contracted (f) AFP EM map.